ORIGINAL ARTICLE

Prediction and analysis of grinding force on grinding heads based on grain measurement statistics and single-grain grinding simulation

Baichun Li[1] · Xiaokun Li[1] · Shenghui Hou[1] · Shangru Yang[1] · Zhi Li[1] · Junze Qian[1] · Zhenpeng He[1]

Abstract

Reliable prediction of the grinding force is essential for improving the grinding efficiency and service life of the grinding head. To better optimize and control the grinding process of the grinding head, this paper proposes a grinding force prediction method of the grinding head that combines surface measurement, statistical analysis, and finite element method (FEM). Firstly, a grinding head surface measurement system is constructed according to the principle of focused imaging. The distribution model of abrasive grains in terms of size, spacing, and protruding height has been established by measuring and counting the characteristics of abrasive grains on the surface of a real grinding head. Then, the undeformed chip thicknesses when the abrasive grains are cut are analyzed in depth, the material model of abrasive grains and workpiece is established, and the cutting process of abrasive grains with different characteristics on the surface of the grinding head is analyzed by finite element simulation. A single abrasive grain grinding force model is obtained. Finally, the grinding force prediction of the grinding head was realized by combining finite element simulation with grinding kinematics analysis. In addition, grinding experiments with different grinding parameters were conducted to verify the grinding force prediction model. The results show that the predicted grinding force of the grinding head is in good agreement with the experimental values. The average error of tangential grinding force is 7.42%, and the average error of normal grinding force is 9.77%. This indicates that the grinding force prediction method has good accuracy and reliability.

Keywords Grinding force · Statistical model · Grinding head · Finite element method · Grain-workpiece contact

1 Introduction

Grinding is widely used in aerospace, automotive, biomedical, and other industries as a necessary technical means of machining parts [1]. Its essence is to obtain a higher quality workpiece surface by the interference between the workpiece and multiple abrasive grains on the surface of the grinding head. Grinding force is an essential feature of the grinding process that significantly influences the integrity of the machined surface, the material removal rate, and the life of the grinding head. It is related to almost all grinding parameters [2]. Suppose the magnitude of the grinding force can be accurately predicted before the grinding process to reduce the time and cost of experimentation. In that case, it

will be significant in optimizing the grinding parameters and improving the machined surface quality.

The shape, distribution, size, and attitude of the abrasive grains on the grinding head surface are highly randomized, making it very difficult to predict the grinding force. Compared with the grinding head, research on the grinding wheel is more extensive. Due to the similar structure between grinding wheels and grinding heads, the research results on grinding wheels can be used as reference for predicting the grinding force of grinding heads. Early scholars mainly established empirical models to predict grinding force, which requires a series of grinding experiments under specific conditions to develop the mathematical regression equation between the input parameters and the output results to predict the grinding force [3, 4]. This prediction model has some technical value but requires many experiments to construct the regression equation.

With the development of computer technology, some scholars apply the ideas of big data and machine learning to

✉ Xiaokun Li
1286844926@qq.com

1   College of Aeronautical Engineering, Civil Aviation
    University of China, Tianjin 300300, China

the prediction of grinding force. Fuh et al. [5] proposed to improve the back propagation neural network with an error distribution function and applied it to predict the grinding force, which was more accurate than the theoretical force model. Zhou et al. [6] established a titanium alloy grinding force prediction model based on a back-propagation neural network BP model and a genetic algorithm optimized back-propagation neural model, and its accuracy is much higher than the traditional regression equation prediction results. Zhang et al. [7] established a grinding force model based on a multi-exponential function, and the results showed that the model could accurately predict the grinding force for unidirectional grinding of composites. This method also needs to analyze a large number of experimental data to achieve the prediction of grinding force.

In addition to empirical models, there are many analytical and semi-analytical models for predicting grinding forces. Scholars divide the grinding process into three stages: friction, plowing, and cutting and use chip thickness, friction coefficient, and stress coefficient to solve the magnitude of grinding force [8–11]. Hecker et al. [12] assumed that abrasive grain heights follow a Rayleigh distribution, developed a probabilistic model of undeformed chip thickness, and applied it to a grinding force prediction model. Durgumahanti et al. [13] considered the effect of machining parameters and friction coefficients and developed mathematical models of grinding force per unit width for each of the three grinding phases. The results were more in agreement with the experiments. Dai et al. [14] found that the undeformed chip thicknesses of single-layer CBN grinding wheel satisfy the regular distribution by conducting several grinding experiments and establishing the grinding specific force and specific energy models. Li et al. [15] combined the empirical formulas and the theoretical derivations to analyze the forces in the three grinding stages based on the conical grain model. They established a grinding force prediction model in which the friction force accounted for the central part of the grinding force. This prediction model ignores the actual grinding process and is easy to cause errors.

To more accurately predict the grinding force and reveal the material removal mechanism, more and more scholars focus on the single-grain cutting process and analyze the kinematic model of grain-workpiece interaction based on the analytical model [16–18]. Li et al. [19] considered the protruding heights of different abrasive grains and the interference state between the abrasive grains and the workpiece at each moment. They found that friction and cutting are the two main phases among the three phases of grinding and established a grinding force prediction model based on the analytical model of friction force, plowing force, and cutting force. Jamshidi et al. [20] considered the microscopic mutual interference between the abrasive grains and the workpiece. They found that the abrasive grains with negative rake angles would form the dead metal zone (DMZ) with the workpiece and constructed a grinding force prediction model considering the dead metal zone (DMZ). Wang et al. [21] obtained the grinding specific energies corresponding to different undeformed chip thicknesses through single-grain grinding experiments. They constructed a grinding force prediction model by combining it with the single-grain grinding force model, and the results were more consistent with the experiments. Meng et al. [22] considered the distribution, attitude, shape, and size of abrasive grains on microstructured tools to develop a dynamic grinding force prediction model based on abrasive grain kinematics. Wu et al. [23] simplified the abrasive grains to a spherical shape, analyzed the instantaneous undeformed chip thickness of the abrasive grains by kinematic simulation, and combined it with the material contact mechanics to achieve the prediction of the grinding force.

However, the empirical model requires a lot of grinding experiments to obtain the grinding force prediction model, and the grinding force prediction model needs to be updated when the working conditions change, which will waste a lot of time and economic cost. Many analytical and semi-analytical models ignore many characteristics of the actual grinding process, such as the distributions of abrasive grains on the surface of the grinding head, the contact area between the abrasive grains and the workpiece, the material properties of the grinding head and the workpiece, and the actual process of the abrasive grains cutting the workpiece [24], which can lead to errors in the grinding force prediction. On the other hand, analytical and semi-analytical models are cumbersome to calculate, and it is difficult to analyze and discuss the grinding process by purely theoretical analysis and experimental methods.

Therefore, in this paper, the size, protruding height, and distribution of abrasive grains on the grinding head surface are measured and counted by the microfocus 3D reconstruction system. Then, the grinding process of different abrasive grains is simulated and analyzed using finite elements based on the actual topography of the grinding head surface. The finite element method can intuitively and accurately respond to the actual interference process between the abrasive grains and the workpiece, and its consideration of the material properties of the workpiece can provide a more realistic grinding force. From the simulation, the grinding force values of single grains are extracted and combined with the effective number of grains in the grinding arc area to realize the grinding force prediction. Finally, the accuracy of the prediction model is verified by grinding experiments. The grinding force prediction model obtained by this method will be more in line with the actual grinding process, and the method has better engineering practical significance.

2 Measurement and modeling of the grinding head surface based on focused imaging

The characteristics of the abrasive grains on the grinding head surface are critical factors affecting the grinding force, including the shape, size, number, position, and protruding height of the abrasive grains. To accurately predict the grinding force of the grinding head, measuring and analyzing the abrasive grains on the grinding head surface is necessary. Usually, an optical microscope can only observe the 2D parameters of the abrasive grains on the grinding head surface, and the 3D information of the abrasive grains cannot be obtained. For this reason, this paper builds a measurement and 3D reconstruction system of the grinding head surface based on focusing imaging.

2.1 The principle of focused imaging measurement

According to the microscopic focusing imaging principle [25], the collimation plane of the optical measurement system is fixed and unique. Its distance from the lens is μ, as shown in Fig. 1. When the grinding head is in the initial position, the positions on the surface of the grinding head within the depth of field ΔT centered on the focal plane z_1 are clearly imaged, and the rest of the positions are blurred. By moving the distance between the grinding head and the lens in micrometer steps Δz, the surface of the grinding head at different height positions is focused on the newly acquired image, and an image sequence of the grinding head surface acquired at equal distances in the direction of the height of the abrasive grains can be obtained. The best-focused image position of each pixel point is determined by calculating the focus value of each pixel in each image frame. Then, by combining the best-focused image positions of all pixel points on the grinding head surface with their position

information in the height direction, height information on the topography of the grinding head can be obtained.

As shown in Fig. 2, the primary processes of the grinding head surface measurement based on focus imaging are acquiring n_k grinding head surface images at equal intervals to obtain a sequence of grinding head surface images, Using the focus sharpness function to calculate the focus value E of each pixel point in the image and fitting the focus value curve to calculate the number of image frames f_k corresponding to the maximum focus value E_{max}. According to the mapping relationship between the number of image frames and the height information of the focused pixel point, the height information matrix is established. Then, the 3D surface topography of the grinding head can be reconstructed precisely by combining with the 2D information of the image.

2.2 Statistical modeling of abrasive grains

In order to analyze the distribution of abrasive grain characteristics on the grinding head surface, a 100# electroplated CBN grinding head was used as the object of study. Twelve areas of the grinding head surface, selected randomly along the periphery, were measured, and the number of abrasive grains in each area is shown in Fig. 3 (172 abrasive grains total). The number of abrasive grains in the unit area is shown as:

$$n_a = \frac{N}{S_r} \tag{1}$$

where S_r is the total area of the selected region, and N is the total number of abrasive grains in the selected region. By using an optical microscope to observe the shape of the abrasive grains on the grinding head surface, it can be found that the abrasive grains in the form of the triangular platform account for more than 65%. While ensuring that the abrasive particle model on the grinding tool surface closely
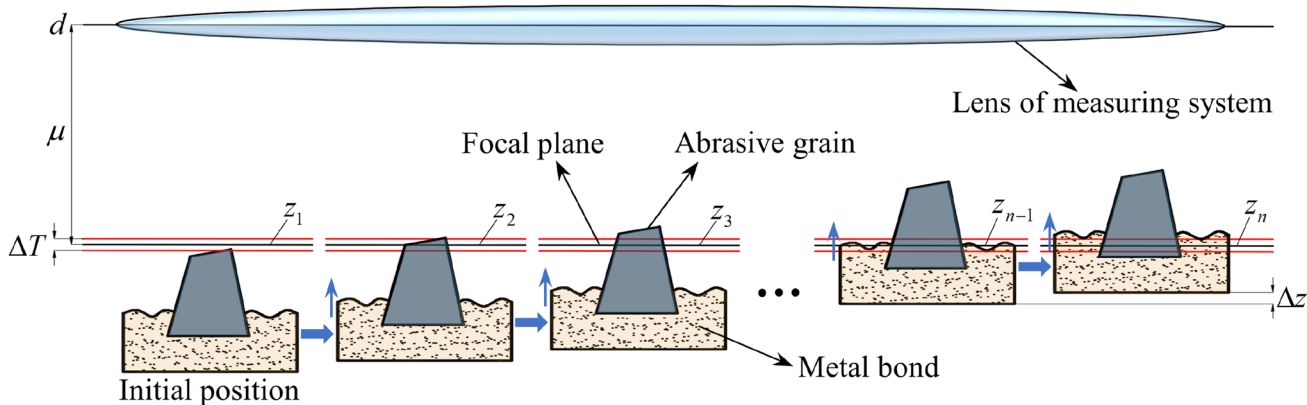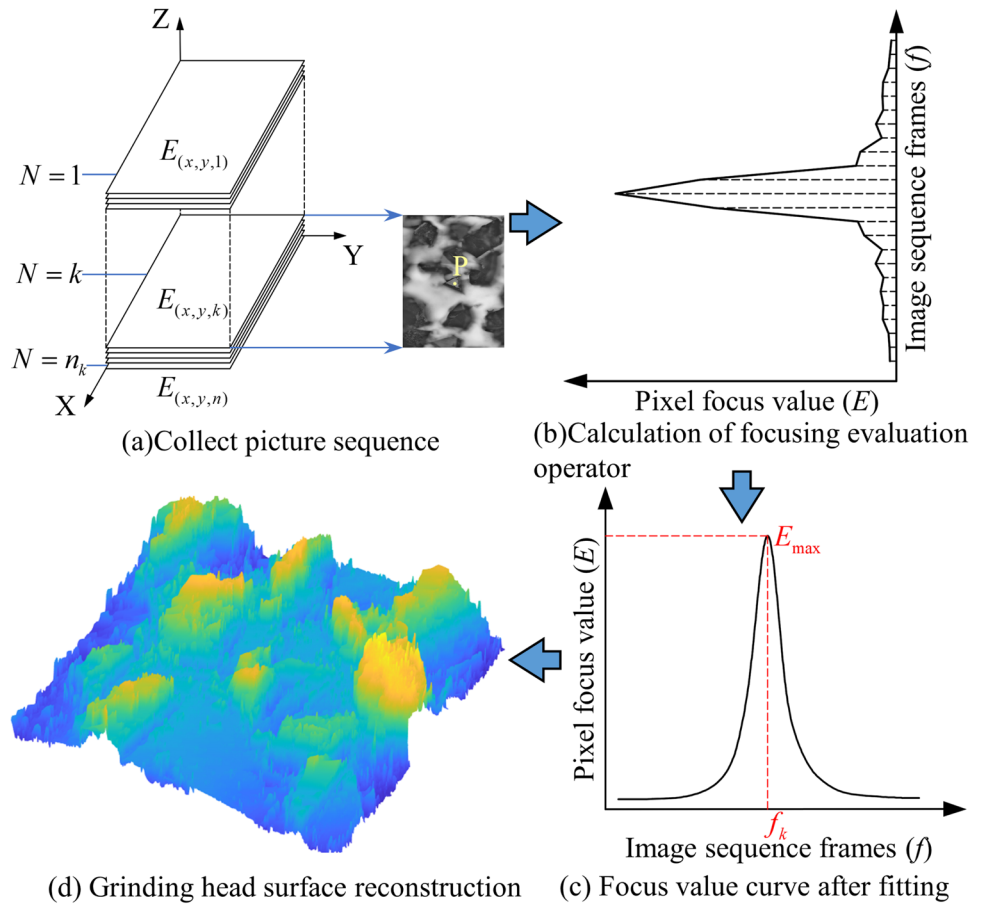

Fig. 1 Principles of microscopic focusing measurement

Fig. 2 The primary processes of micro-focusing measurement

(a) Collect picture sequence

(b) Calculation of focusing evaluation operator

(c) Focus value curve after fitting

(d) Grinding head surface reconstruction

approximates the actual surface, this study assumes that the shape of the abrasive particles on the grinding tool surface is the regular triangular platform to facilitate calculation and analysis.

The distribution spacing L of the abrasive grains affects the number of abrasive grains involved in cutting during the grinding transition and changes the magnitude of the grinding force. In order to obtain the distribution patterns of abrasive grain spacings, the spacings between the abrasive grains in each of the 12 regions were measured using an optical microscope. After statistical analysis, the distribution pattern satisfies the normal distribution, and the mean value is calculated to be 141.08 μm, and the standard deviation is calculated to be 27.41 μm. The fitting results are shown in Fig. 4.

Abrasive grain sizes are related to the specifications of the grinding head and are generally measured by the minimum outer ball diameter. Since the abrasive grains on the surface of the grinding head are held in place by the bonding agent and cannot be rotated in 3D space to measure the minimum outer ball diameter, this paper takes the minimum outer circular diameter D_g of the abrasive grains measured on the 2D plane as the abrasive grain sizes, as shown in Fig. 5. The abrasive grain sizes on a single grinding head usually vary within a specific range. The abrasive grain sizes in each of

the above 12 regions are measured by optical microscopy. As shown in Fig. 6, the statistical analysis shows that the abrasive grain sizes roughly follow the normal distribution law, with the mean and standard deviation of 138.6 μm and 19.2 μm, respectively, and the fitting results are shown in Fig. 6.

The protruding height of the abrasive grain h is an essential parameter of the grinding head surface, and the ordinary optical microscope can only obtain the parameters of the abrasive grain surface, but not the depth information. In order to measure the protruding heights of the abrasive grains, this paper builds a measurement and 3D reconstruction system of grinding head surface based on focused imaging, as shown in Fig. 7, which controls the grinding head to move along the z-axis at micrometer level by servomotor, so that the acquisition system traverses the whole abrasive grain in the height direction, reconstructs the surface topography of the grinding head, and realizes the measurement of the height of the abrasive grain. The 12 regions were reconstructed using this measurement system, as shown in Fig. 8a. Comparison with the actual image shows that the shape and position of the reconstructed abrasive grains are the same as those of the real abrasive grains. The maximum feature size difference between the reconstructed and actual abrasive grains is within 2 μm, and the maximum distribution error
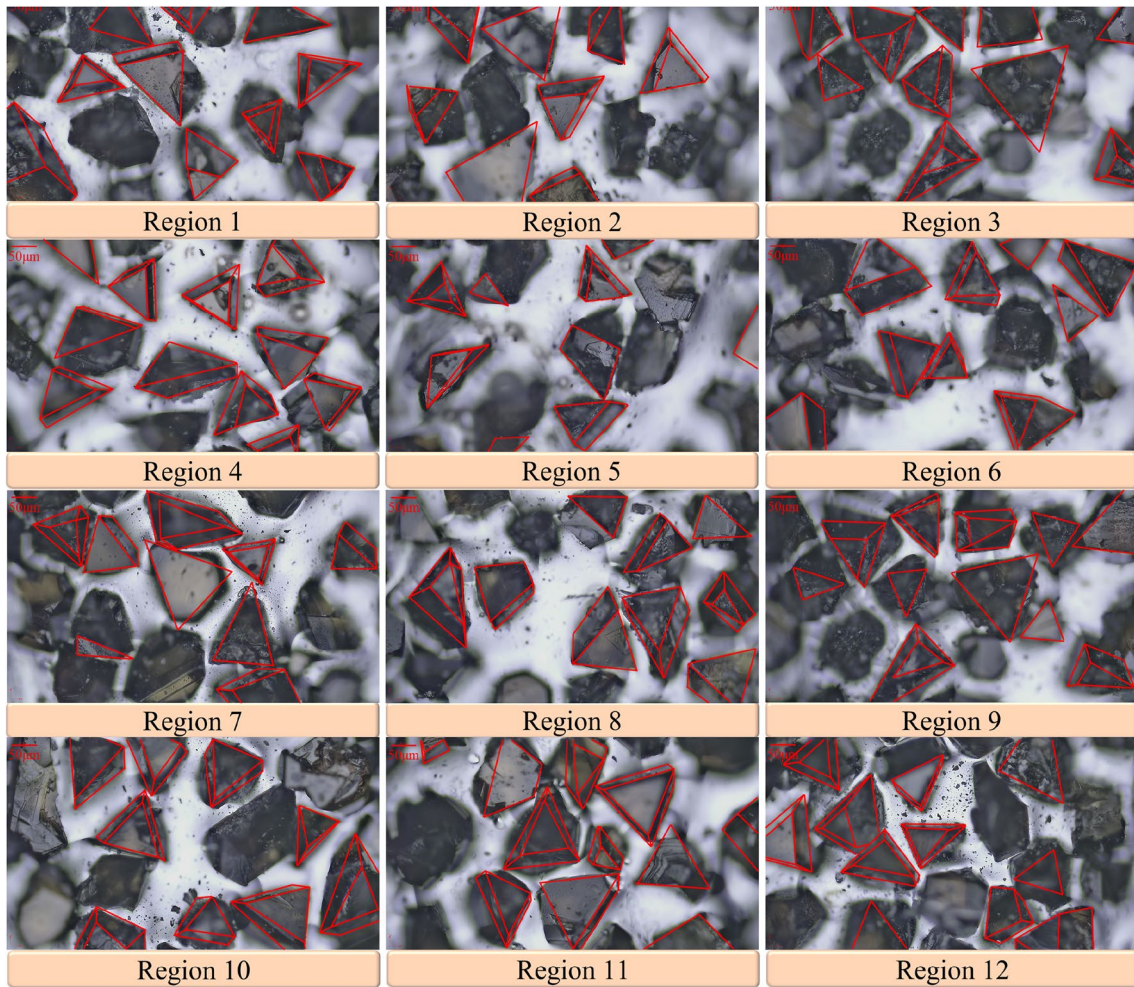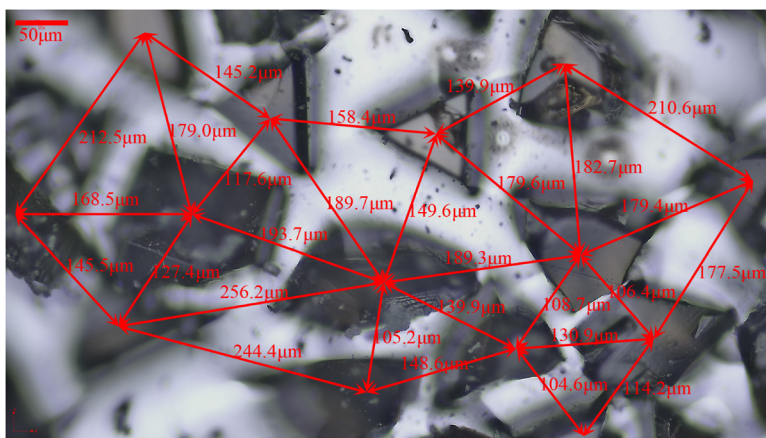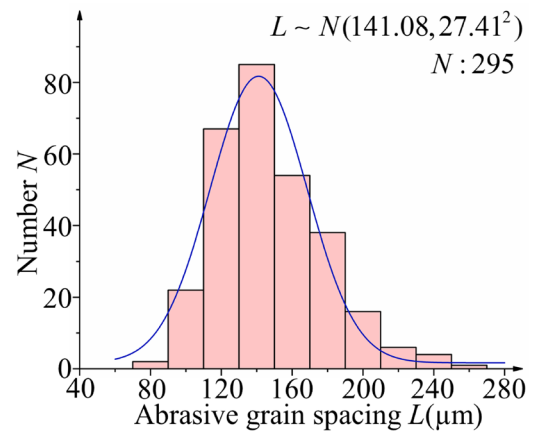
Fig. 3 The surface morphology of electroplated CBN grinding head

(a) Measurement of abrasive grain spacing

(b) Distribution of abrasive grain spacing

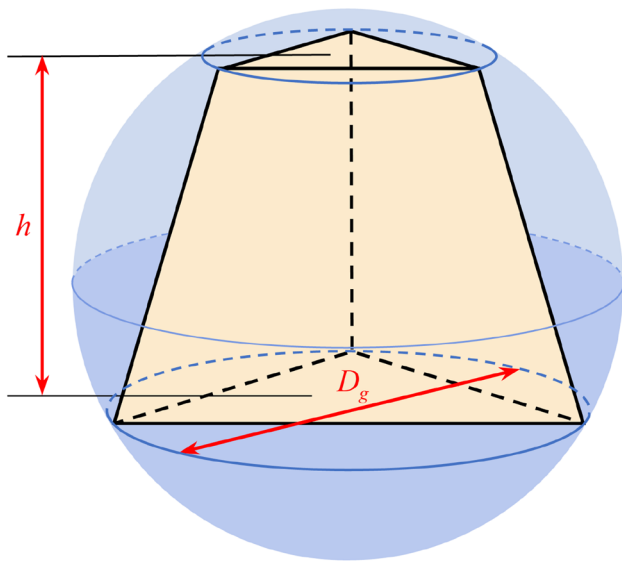**Fig. 4** The distribution pattern of abrasive grain spacing

Fig. 5 The schematic diagram of abrasive grain size

is within 3 μm. The measurement reconstruction system can accurately reconstruct the geometric features and positional distribution of the abrasive grains in the grinding head. Statistical analysis of the protruding heights of all abrasive grains, as shown in Fig. 8b, shows that the distribution conforms to the normal distribution, and the mean and standard deviation are 39.34 μm and 12.14 μm, respectively.

3 Grinding force modeling

The essence of grinding is to interfere with the workpiece through the mutual coupling of multiple abrasive grains on the surface of the grinding head, and the collection of forces generated by each abrasive grain, as it interferes with the workpiece, constitutes the grinding force of the grinding head. By analyzing the magnitude of the force generated by each abrasive grain, a grinding force predictive model of the grinding head during the actual grinding process can be established. Unlike the previous models, this model is obtained by the finite element simulation method to get the force generated when a single abrasive grain interferes with the workpiece, which considers the material properties of the workpiece during the interference process and makes the result analysis more accurate, intuitive, and realistic. In addition, the modeling considers the geometric characteristics, the distribution spacing, and the actual grinding thickness of the abrasive grains on the grinding head surface, which can reflect the real grinding process and provide a more accurate prediction of the grinding force.

3.1 Undeformed chip analysis

There are several abrasive grains distributed on the grinding head surface, but not all of them can interfere with the workpiece, which depends on the grinding depth and the protruding height of the abrasive grains. As shown in Fig. 9, the grinding depth a_p is generally based on the maximum protruding height of the abrasive grain h_{max}. The grinding depth must be specified before machining, and the abrasive grain can interfere with the workpiece only when the protruding height of the abrasive grain h satisfies Eq. 2. This part of the abrasive grains is called active abrasive grains:

$$h_{max} - a_p \le h \le h_{max} \tag{2}$$

As the grinding depth increases, the number of active abrasive grains increases. When the grinding depth increases to
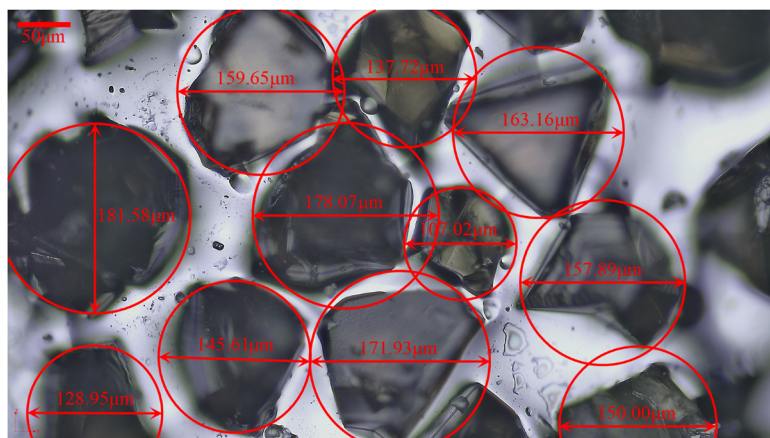
(a) Measurement of abrasive grain size
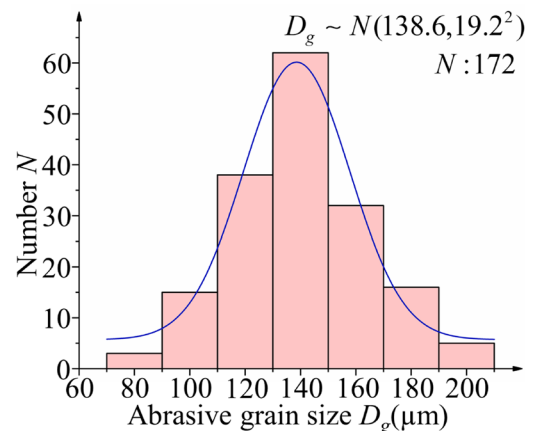
(b) Distribution of abrasive grain size

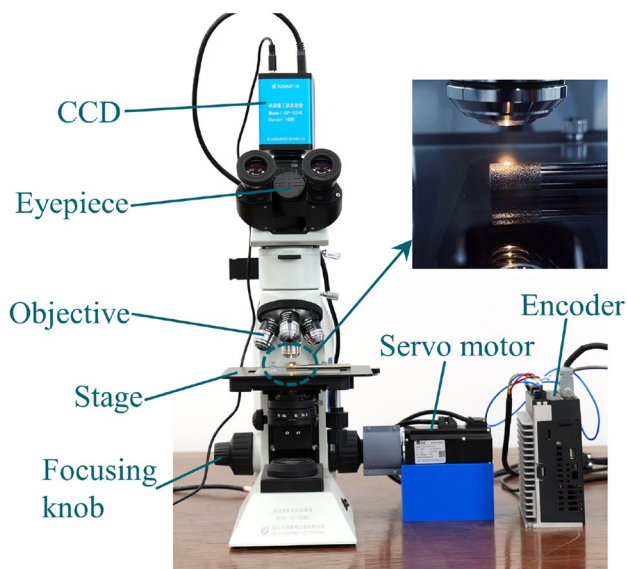**Fig. 6** The distribution pattern of abrasive grain size

Fig. 7 The grinding head surface measurement and reconstruction system

the lowest abrasive grain interference depth, the number of active abrasive grains reaches the maximum, and because the total number of abrasive grains on the surface of the grinding head is limited, at this time, the grinding depth continues to increase, and the number of active abrasive grains remains unchanged.

The actual thickness of a single abrasive grain when interfering with the workpiece is characterized by the maximum undeformed chip thickness h_m (abrasive grain depth of cut), which varies with the protruding height of the abrasive grain. In order to easily calculate the maximum undeformed chip thickness h_m, the cutting path of the abrasive grain can be approximated by a circular arc, as shown in Fig. 10a. The abrasive head moves from point O to point O', then the maximum undeformed chip thickness h_m can be expressed as:

$$h_m = AC = O'C - O'A = \frac{d_s}{2} - O'A = \frac{d_e + 2h}{2} - O'A \quad (3)$$

where d_s is the diameter of the abrasive grain at the instant of rotation, and d_e is the diameter of the grinding head. Assuming that the abrasive grains are arranged at intervals L along the circumference of the grinding head, the distance s that the cutting path of the previous abrasive grain travels along

Fig. 8 The distribution pattern of abrasive grain protruding height

(a) Comparison between reconstructed surface and actual surface of grinding head

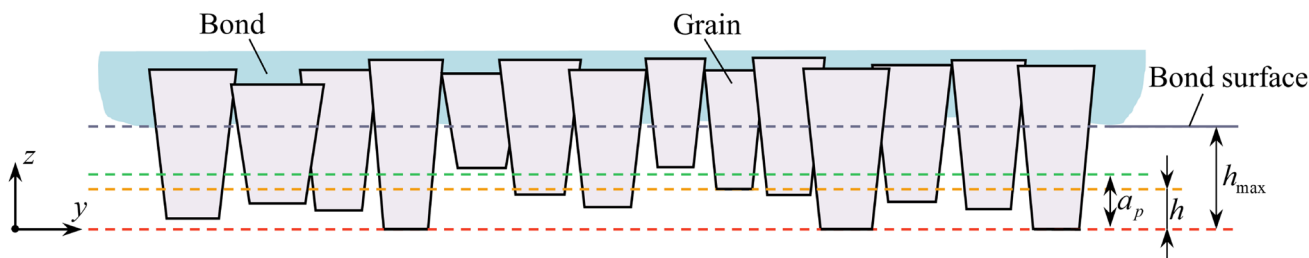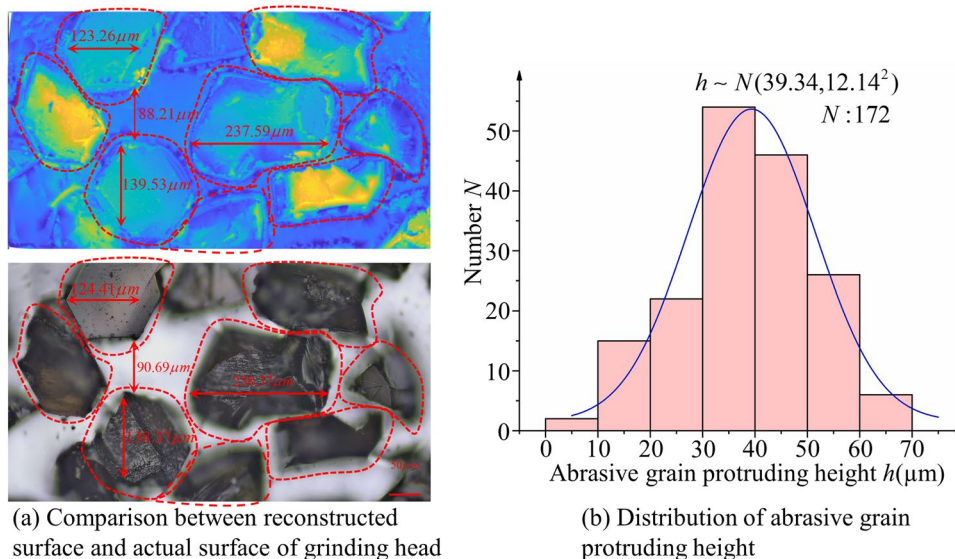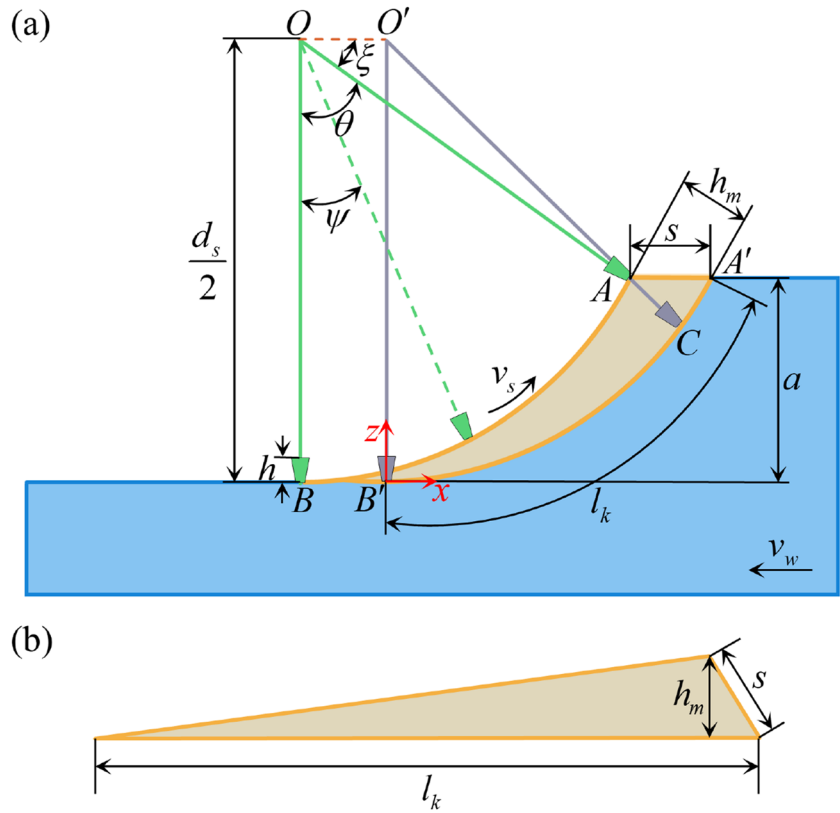(b) Distribution of abrasive grain protruding height

Fig. 9 The distribution of abrasive grain on the surface of the grinding head

Fig. 10 Schematic diagram of the abrasive grain cutting process: **a** abrasive grain interfering with the workpiece process; **b** undeformed chip geometry

the feed direction can be expressed as the product of the interval time t_e between two successive cuts and the workpiece feed speed v_w:

$$s = OO' = \frac{Lv_w}{v_s} \tag{4}$$

where v_s is the linear velocity of the grinding head, and in $\triangle OO'A$, the length of $O'A$ can be expressed as:

$$O'A = \left(OA^2 + OO'^2 - 2 \cdot OA \cdot OO' \cdot \cos\xi\right)^{1/2} = \left[\left(\frac{d_s}{2}\right)^2 + s^2 - sd_s\cos\xi\right]^{1/2} \tag{5}$$

where ξ is the angle between OO' and OA, and

$$\cos\xi = \left(1 - \cos^2\theta\right)^{1/2} \tag{6}$$

In $\triangle OAB$, there is $\cos\theta = 1 - 2a/d_s$, which can be substituted into Eq. 6 to obtain the following:

$$\cos\xi = \left(1 - \left(1 - \frac{2a}{d_s}\right)^2\right)^{1/2} \tag{7}$$

where a is the depth at which abrasive grain can interfere with the workpiece, and $a = a_p - h_{\max} + h$, substituting Eq. 7 into Eq. 5 follows:

$$O'A = \left(\frac{d_s}{2}\right)\left[1 - \left(\frac{8s}{d_s}\left(\frac{a}{d_s}\right)^{1/2}\left(1 - \frac{a}{d_s}\right)^{1/2} - \frac{4s^2}{d_s^2}\right)\right]^{1/2} \tag{8}$$

Due to $a \ll d_s$ and $s \ll d_s$, the second term in the brackets in Eq. 8 is much smaller than unity. Then, the equation can be simplified as:

$$O'A = \left(\frac{d_s}{2}\right)\left(1 - \left(\frac{4s}{d_s}\left(\frac{a}{d_s}\right)^{1/2}\left(1 - \frac{a}{d_s}\right)^{1/2} - \frac{2s^2}{d_s^2}\right)\right) \tag{9}$$

After substituting Eq. 9 into Eq. 3, it can be concluded as follows:

$$h_m = 2s\left(\frac{a}{d_s}\right)^{1/2}\left(1 - \frac{a}{d_s}\right)^{1/2} - \frac{s^2}{d_s} \tag{10}$$

Due to $a \ll d_s$, $a/d_s \ll 1$, the maximum undeformed chip thickness h_m can be as follows:

$$h_m = 2s\left(\frac{a}{d_s}\right)^{1/2} - \frac{s^2}{d_s} \tag{11}$$

After determining the maximum undeformed chip thickness h_m for each grain on the grinding head surface, it is

used as the abrasive grain cutting thickness for finite element simulation to obtain the grinding force when the single abrasive grain cuts.

3.2 Simulation modeling of single abrasive grain grinding force

In this study, the interaction process between the abrasive grain and the workpiece was simulated using ABAQUS/Explicit simulation software, and the grinding force model for a single abrasive grain was analyzed. It is worth noting that this study did not focus on the deformation/fracture of the abrasive grains, so the abrasive grains were considered rigid bodies in the simulation.

3.2.1 Modeling

According to the analysis in Sect. 2.2, the shape, size, position, and protruding height of the abrasive grains on the surface of the grinding head have a high degree of randomness. In order to simplify the simulation analysis, it is assumed that the shape of the abrasive grains is the regular triangular platform, and the abrasive grains are arranged at intervals of 200 μm in the circumferential direction of the grinding head. The attitudes of the abrasive grains around the z-axis change periodically, as shown in Fig. 11. When the rotational speed of the grinding head is different, the cutting speed of the abrasive grains is also different, which will lead to different forces generated by the abrasive grains cutting the same thickness of the workpiece, so different rotational speeds of the grinding head must be analyzed separately, and the parameters of the single abrasive grain cutting simulation are shown in Table 1. Randomly selected abrasive grains of different sizes, attitudes, and protruding heights are used as tools for finite element simulation. It is worth noting that the cutting edges of the abrasive grains at the macro scale are generally considered sharp, while at the microscale, considering the manufacturing and wear of the abrasive grains, the cutting edges of the simulation model are bluntly rounded.

The maximum undeformed chip thickness h_m for abrasive grain grinding can be calculated from Eq. 11. According to Fu et al. [26], it can be seen that the actual undeformed chip thickness increases slowly along the cutting path to the maximum value h_m and then decreases sharply to zero, as shown in Fig. 10b, and its grinding force varies approximately linearly. Since the workpiece model h_m is very small, it is difficult to mesh, so the workpiece is simplified as an ortho-hexahedron for orthogonal cutting simulation. At this time, the grinding force obtained is the maximum in the abrasive grain cutting process, and after that, the fitting can be approximated to obtain the process of changing the grinding force.

3.2.2 Material properties

Inconel 718 has good corrosion resistance, thermal stability, and thermal fatigue properties at high temperatures and has been widely used in many fields, such as aerospace, aviation, and naval vessels [27]. CBN abrasives have better machining performance in grinding nickel-based superalloy, especially at higher grinding speeds [28]. Compared with other abrasive materials, CBN has excellent thermal conductivity, thermal stability, and wear resistance [29]. In this paper, Inconel 718 material is used as the machining workpiece,

Table 1 Simulation parameters for single abrasive grain cutting

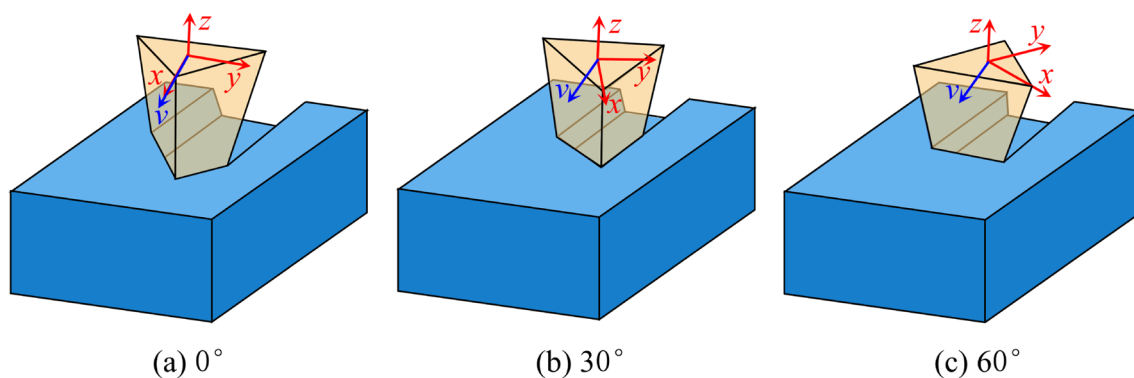| Simulation parameters	Value
Cutting speed (mm/s)	840
Depth of cut (μm)	0.1023, 0.1178, 0.1314

Fig. 11 Schematic diagrams of abrasive cutting in different attitudes

and the CBN grinding head is used as the machining tool. The physical properties of CBN and Inconel 718 material are shown in Table 2 [30].

The constitutive model of the workpiece material is used to describe the relationship between stress and strain, and the selection of the constitutive model in the grinding process affects the state of the workpiece material, which in turn affects the magnitude of the grinding force. In metal material cutting simulation, the J-C constitutive model can better reflect the behavior of metal materials and can accurately reproduce the cutting workpiece process [31]. The model expresses the material yield stress as follows:

$$\sigma = \left[A + B(\varepsilon)^n \right] \left[1 + c \ln \left(\frac{\dot{\varepsilon}}{\dot{\varepsilon}_0} \right) \right] \left[1 - \left(\frac{T - T_r}{T_m - T_r} \right)^m \right] \quad (12)$$

where A, B, c, m, n are determined by the material property, A is the initial yield strength of the material, B is the hardening constant of the material, c is the strain rate coefficient of the material, m is the thermal softening index of the material, n is the hardening index of the material, ε is the equivalent plastic strain of the material, $\dot{\varepsilon}$ is the equivalent plastic strain rate, $\dot{\varepsilon}_0$ is the reference plastic strain, T is the instantaneous temperature of the material during grinding, T_r is the ambient temperature, and T_m is the melting point of the material.

In addition to the constitutive model of the workpiece material, the selection of the failure criterion affects the chip formation and the grinding force value of grinding. During the grinding process, the workpiece undergoes elastic-plastic deformation by extruding abrasive grains, and when the deformation of the workpiece reaches a critical value, damage fracture occurs, and chips are formed. To simulate this process, the J-C failure model in the simulation process adopts the fracture equivalent plastic strain $\overline{\varepsilon}_f$. The failure parameter w determines the failure criterion, and the expression is as follows:

$$\begin{cases} \overline{\varepsilon}_f = \left[D_1 + D_2 \exp\left(D_3 \frac{P}{q} \right) \right] \left[1 + D_4 \ln \left(\frac{\dot{\overline{\varepsilon}}}{\dot{\overline{\varepsilon}}_0} \right) \right] \left[1 + D_5 \ln \left(\frac{T - T_m}{T_m - T_r} \right) \right] \\ w = \sum \left(\frac{\Delta \overline{\varepsilon}}{\overline{\varepsilon}_f} \right) \end{cases}$$
$$(13)$$

where $\overline{\varepsilon}_f$ is the equivalent plastic fracture strain; D_1, D_2, D_3, D_4, D_5 are the failure constants at room temperature; and $\dot{\overline{\varepsilon}}$ is the equivalent plastic strain rate; $\dot{\overline{\varepsilon}}_0$ is the equivalent reference strain rate; P is the compressive stress; q is the equivalent stress, and $\Delta \overline{\varepsilon}$ is the equivalent plastic strain increment for each incremental step.

When the workpiece material is damaged and fractured, the workpiece's load-bearing capacity and deformation resistance are gradually reduced, eventually leading to material failure. In order to simulate this damage process, it is necessary to use the damage evolution criterion based on the equivalent plastic strain increment based on the J-C damage criterion. The damage parameter d in the damage evolution criterion can describe the degree of stiffness degradation, which usually has a linear, tabular, or exponential relationship with the equivalent plastic strain increment $\overline{u}_f$. In the case of linear evolution, the expression of the damage parameter d is as follows:

$$\dot{d} = \frac{I\dot{\overline{\varepsilon}}}{\overline{u}_f} = \frac{\dot{\overline{u}}_f}{\overline{u}_f} \quad (14)$$

where I is the characteristic length of the cell grid. When $d = 1$, it indicates that the workpiece material has been destroyed and is in a failed state. At this point, the element mesh is deleted, and $\overline{u}_f$ is defined as the failure displacement at the time of material failure, which can be expressed as:

$$\overline{u}_f = I\dot{\overline{\varepsilon}} \quad (15)$$

Erice et al. [30] proposed the J-C constitutive model and damage parameters for Inconel 718 material, as shown in Tables 3 and 4.

3.2.3 Analysis of single-grain grinding simulation results

Different abrasive grain sizes (100, 120, and 140 μm), different abrasive grain protruding heights (40, 50, and 60 μm), and different angles (0°, 30°, and 60°) were selected as cutting tools for orthogonal cutting simulation. As shown in Fig. 12, the variation curves of the grinding force when a single abrasive grain (abrasive grain size of 140

Table 2 Physical properties of CBN and Inconel 718 materials

Material	Inconel 718	CBN
Density (kg/m^3)	8220	3400
Young's modulus (GPa)	208	710
Poisson's ratio	0.3	0.15
Heat conductivity (W/(m K))	11.4	80
Specific heat capacity (J/(kg K))	203	430
Linear expansion coefficient (K^{-1})	1.3×10^{-5}	2.2×10^{-6}

Table 3 J-C constitutive model parameters for Inconel 718

Parameter	Value
A (MPa)	1200
B (MPa)	1284
c	0.006
n	0.54
m	1.2

Table 4 J-C damage model parameters for Inconel 718

Parameter	Value
D_1	0.04
D_2	0.75
D_3	− 1.45
D_4	0.04
D_5	0.89

μm, protruding height of 50 μm, and angle of 0°) cuts the workpiece.

In the initial contact stage, the blunt round cutting edge continuously squeezes the workpiece, the workpiece at the leading edge of the abrasive grain undergoes elastic-plastic deformation to form a bulge, and the squeezing and plowing behaviors dominate. Until the workpiece is broken, chunky chips are formed at the leading edge, curly chips are formed on both sides of the leading edge, and shearing behavior gradually becomes dominant. The grinding force reaches the maximum value when the abrasive grain is completely cut into the workpiece. Currently, the grinding force is approximately equal to the maximum grinding force in the actual cutting process of the abrasive grain. After that, the abrasive grain is cut out of the workpiece, the grinding force gradually decreases, and the chips are separated from the workpiece.

The simulation results of partially abrasive grain cutting the workpiece are shown in Fig. 13. As the size and protruding height of the abrasive grains increase, the morphology of the deformation area on the workpiece remains relatively consistent. The contact area generates its corresponding chips, but the attitudes of the abrasive grains significantly impact the chip shape. At an angle of 0°,

Fig. 12 Variation curve of the grinding force of a single abrasive grain

the grain comes in contact with the workpiece on both sides and forms identical curly chips. Due to the blunt and rounded cutting edge, the chip does not break in half at the cutting edge. And the workpiece is squeezed by the cutting edge, resulting in chunky chips. At an angle of 30°, the workpiece is primarily squeezed by the side of the abrasive grain. However, the squeezing effect of the two sides of the abrasive grain on the workpiece is different. The left side of the abrasive grain makes initial contact with the workpiece, forming chunky chips with a higher height on the left and a lower height on the right in the contact area. At an angle of 60°, the squeezing effect of the abrasive grain on the workpiece is further enhanced. As a result, a more neatly formed chunky chip is observed in the contact area.

The maximum grinding force generated during the cutting process by abrasive grains with different characteristics varies. It is primarily influenced by the size, attitude, and protruding height of the abrasive grains. The protruding height also affects the maximum undeformed cutting thickness. Based on the previous simulation results, a quadratic polynomial fitting expression can be derived to quickly obtain the maximum grinding force generated by abrasive grains with different characteristics. The expression for fitting the maximum grinding force of abrasive grains with different characteristics is as follows:

$$\mathbf{f}^{\mathrm{T}}(d_g, \alpha, h_m) = \mathbf{G} \cdot \mathbf{X}(d_g, \alpha, h_m) \tag{16}$$

where $\mathbf{f}(d_g, \alpha, h_m) = [f_{F_t}(d_g, \alpha, h_m) \ f_{F_n}(d_g, \alpha, h_m)]$, $f_{F_t}(d_g, \alpha, h_m)$, and $f_{F_n}(d_g, \alpha, h_m)$ represent the maximum grinding forces in the X and Y directions, respectively. $\mathbf{G}$ is a 2×10 coefficient matrix that needs to be calibrated. $\mathbf{X}(d_g, \alpha, h_m) = [d_g^2 \ \alpha^2 \ h_m^2 \ d_g \alpha \ d_g h_m \ \alpha h_m \ d_g \ \alpha \ h_m \ 1]$. To calibrate and calculate the coefficient matrix using the least squares method, Eq. 16 can be rewritten as follows:

$$\mathbf{f}(d_g, \alpha, h_m) = \mathbf{X}(d_g, \alpha, h_m) \cdot \mathbf{G}^{\mathrm{T}} \tag{17}$$

Using maximum likelihood estimation, it can be obtained that:

$$\mathbf{X}^{\mathrm{T}}(d_g, \alpha, h_m) \cdot \mathbf{f}(d_g, \alpha, h_m) = \mathbf{X}^{\mathrm{T}}(d_g, \alpha, h_m) \cdot \mathbf{X}(d_g, \alpha, h_m) \cdot \mathbf{G}^{\mathrm{T}} \tag{18}$$

The coefficient matrix $\mathbf{G}$ to be calibrated can be expressed as:

$$\mathbf{G} = \left((\mathbf{X}^{\mathrm{T}}(d_g, \alpha, h_m) \cdot \mathbf{X}(d_g, \alpha, h_m))^{-1} \cdot \mathbf{X}^{\mathrm{T}}(d_g, \alpha, h_m) \cdot \mathbf{f}(d_g, \alpha, h_m) \right)^{\mathrm{T}} \tag{19}$$

Substituting the size, attitude, and protruding height of the abrasive grains and the simulated grinding forces obtained into Eq. 19:
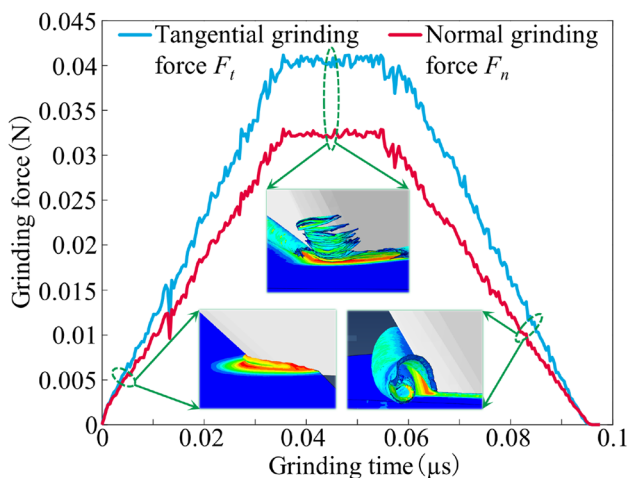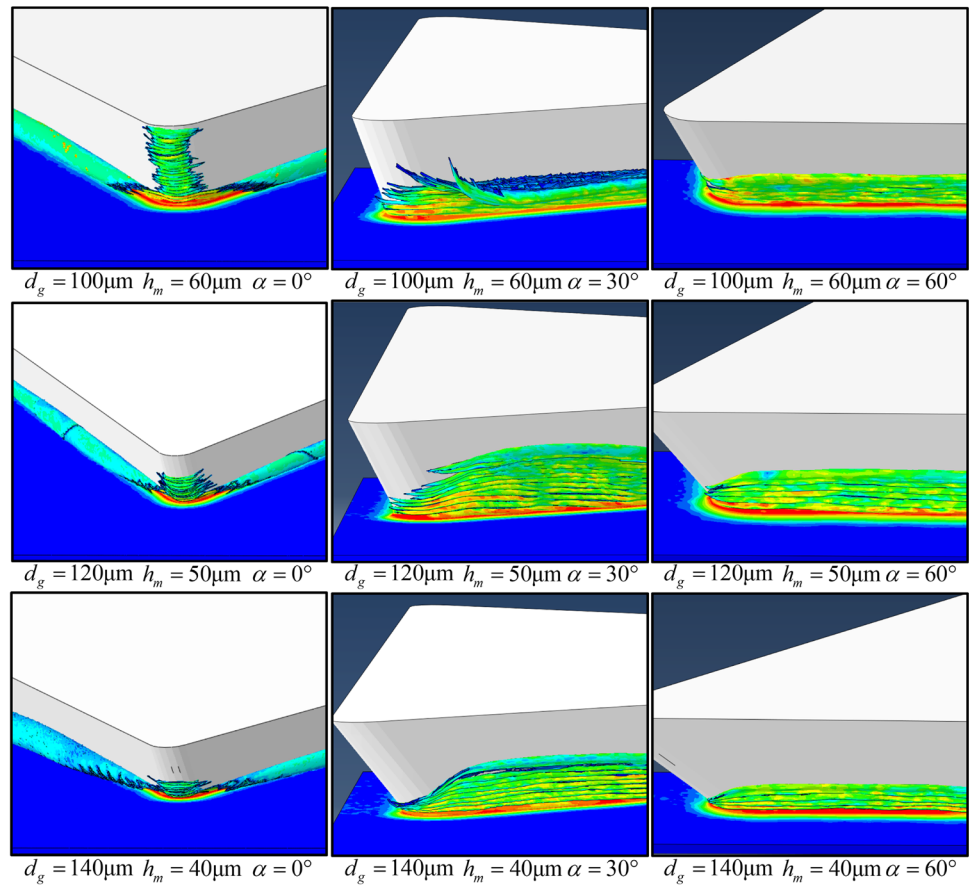
Fig. 13 The simulation results of partially abrasive grain cutting the workpiece

$d_g = 100\mu m \quad h_m = 60\mu m \quad \alpha = 0°$ $d_g = 100\mu m \quad h_m = 60\mu m \quad \alpha = 30°$ $d_g = 100\mu m \quad h_m = 60\mu m \quad \alpha = 60°$

$d_g = 120\mu m \quad h_m = 50\mu m \quad \alpha = 0°$ $d_g = 120\mu m \quad h_m = 50\mu m \quad \alpha = 30°$ $d_g = 120\mu m \quad h_m = 50\mu m \quad \alpha = 60°$

$d_g = 140\mu m \quad h_m = 40\mu m \quad \alpha = 0°$ $d_g = 140\mu m \quad h_m = 40\mu m \quad \alpha = 30°$ $d_g = 140\mu m \quad h_m = 40\mu m \quad \alpha = 60°$

$$
\mathbf{G} = \left(\left(\begin{bmatrix} \mathbf{X}(d_{g1}, \alpha_1, h_{m1}) \\ \mathbf{X}(d_{g2}, \alpha_2, h_{m2}) \\ \vdots \\ \mathbf{X}(d_{gj}, \alpha_j, h_{mj}) \end{bmatrix}^{\mathrm{T}} \cdot \begin{bmatrix} \mathbf{X}(d_{g1}, \alpha_1, h_{m1}) \\ \mathbf{X}(d_{g2}, \alpha_2, h_{m2}) \\ \vdots \\ \mathbf{X}(d_{gj}, \alpha_j, h_{mj}) \end{bmatrix} \right)^{-1} \cdot \begin{bmatrix} \mathbf{X}(d_{g1}, \alpha_1, h_{m1}) \\ \mathbf{X}(d_{g2}, \alpha_2, h_{m2}) \\ \vdots \\ \mathbf{X}(d_{gj}, \alpha_j, h_{mj}) \end{bmatrix}^{\mathrm{T}} \cdot \begin{bmatrix} \mathbf{f}(d_{g1}, \alpha_1, h_{m1}) \\ \mathbf{f}(d_{g2}, \alpha_2, h_{m2}) \\ \vdots \\ \mathbf{f}(d_{gj}, \alpha_j, h_{mj}) \end{bmatrix} \right)^{\mathrm{T}} \tag{20}
$$

Where $\mathbf{X}(d_{gj}, \alpha_j, h_{mj})$ is the vector obtained by substituting the size, attitude, and protruding height of the jth abrasive grain into $\mathbf{X}(d_g, \alpha, h_m)$, and $\mathbf{f}(d_{gj}, \alpha_j, h_{mj})$ is the maximum grinding force obtained from the simulation of the jth abrasive grain. According to Eqs. 16 and 20, the maximum grinding force generated during the cutting process by abrasive grains with any size, attitude, and protruding height can be fitted, as shown in Fig. 14.

3.3 Modeling of grinding force for grinding heads

3.3.1 Kinematic analysis of the grinding process

The area of contact between the grinding head and the workpiece during the grinding process is called the grinding arc region, as shown in Fig. 15, and the area of this region affects the number of abrasive grains momentarily acting on the workpiece. If the deformation of the grinding head and the workpiece is ignored, the area S_e of the grinding head in contact with the workpiece at a given moment is expressed as:

$$S_e = l_e \cdot y_e \tag{21}$$

where l_e is the length of the contact arc between the grinding head and the workpiece, and y_e is the width of the workpiece to be ground by the grinding head. And the contact arc length l_e can be expressed as:

$$l_e = \frac{d_e \delta}{2} \tag{22}$$

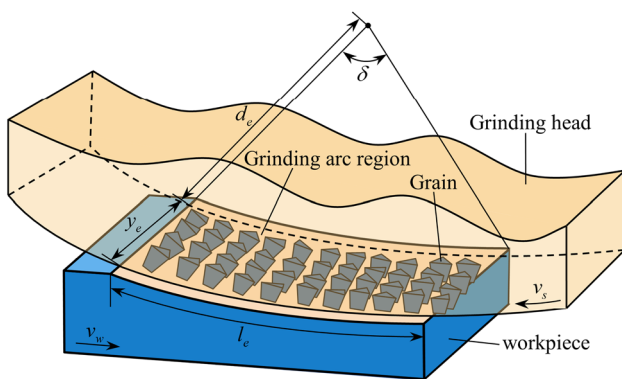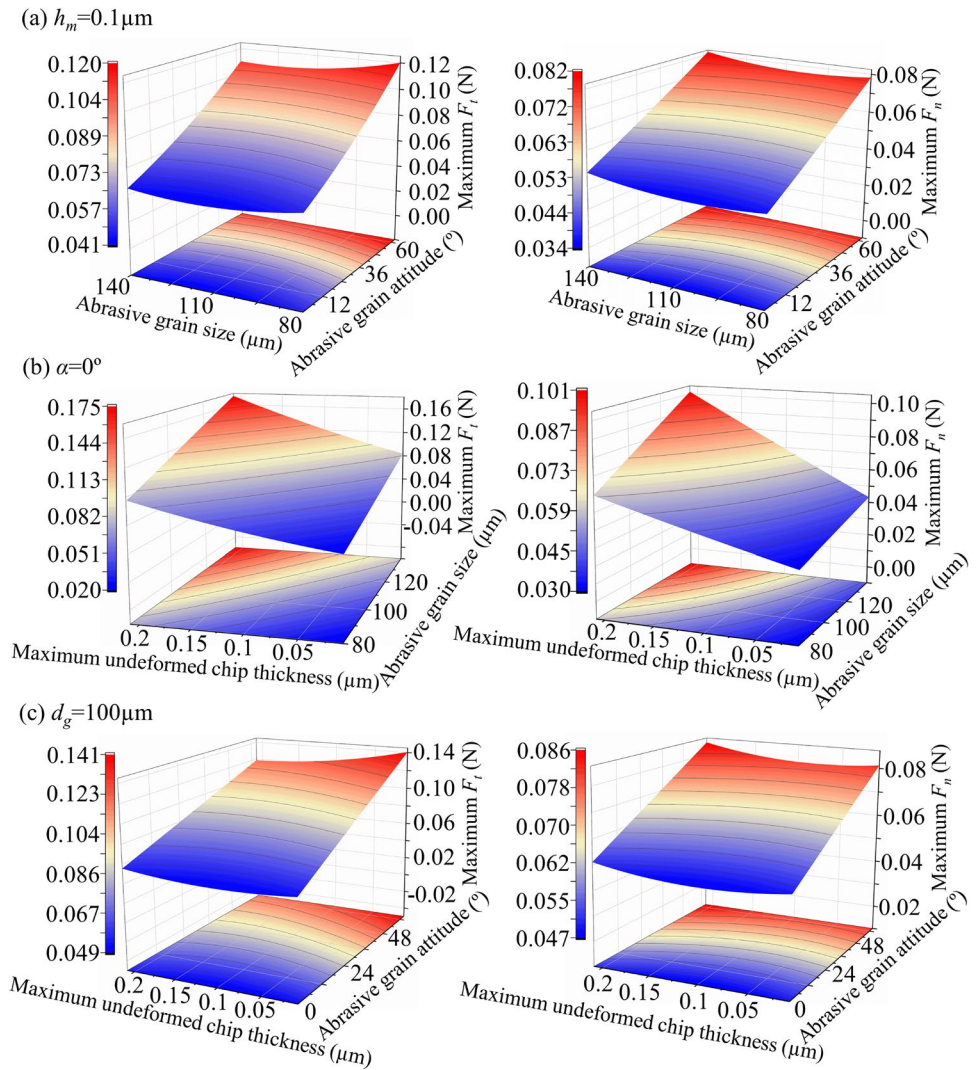**Fig. 14** The maximum grinding force generated by abrasive grains has different characteristics

(a) h_m=0.1μm

(b) α=0°

(c) d_g=100μm

Fig. 15 Grinding head grinding process

where δ is the angle between the arc regions of contact. It can be expressed as:

$$\delta = \arccos\left(1 - \frac{2a_p}{d_e}\right) \tag{23}$$

Since $2a_p \leq d_e$, the approximation can be obtained for small angles:

$$\cos\delta = 1 - \frac{\delta^2}{2} \tag{24}$$

Substituting Eqs. 22, 23, and 24 into Eq. 21 gives

$$S_e = \left(a_p d_e\right)^{1/2} \cdot y_e \tag{25}$$

Combined with the number of abrasive grains in the unit area n_a on the surface of the grinding head in Sect. 2.2, the total number of abrasive grains momentarily in contact with the workpiece in the grinding arc is:

$$n_e = S_e \times n_a \tag{26}$$

The contact arc length l_e is usually referred to as the static contact length between the grinding head and the workpiece. When the motion deformation between the grinding head and the workpiece is considered, as shown in Fig. 10, the actual cutting length l_k of the abrasive grain is called the dynamic contact length, which can be expressed as:

$$l_k = \int_0^\theta dl_k \tag{27}$$

In the $B'XZ$ coordinate system fixed to the workpiece, the trajectory of a single abrasive grain can be expressed as:

$$\begin{cases} x = \frac{d_s}{2}\sin\psi \pm v_w t \\ z = \frac{d_s}{2}(1 - \cos\psi) \end{cases} \tag{28}$$

where ψ is the angle of rotation of the abrasive grain in time t and $t = d_s\psi/2v_s$, "+" stands for reverse abrasion; "−" stands for forward abrasion. Since $\psi < \theta$, then Eq. 28 can be simplified as:

$$\begin{cases} x = \left(1 \pm \frac{v_w}{v_s}\right)\frac{d_s\psi}{2} \\ z = \frac{d_s\psi^2}{4} \end{cases} \tag{29}$$

And dl_k can be expressed as:

$$dl_k = \left[\left(\frac{dx}{d\psi}\right)^2 + \left(\frac{dy}{d\psi}\right)^2 \right]^{1/2} d\psi \tag{30}$$

Substituting Eqs. 29 and 30 into Eq. 27 gives:

$$l_k = \left(1 \pm \frac{v_w}{v_s}\right)\frac{d_s\theta}{2} + \frac{\theta^3}{6\left(1 \pm \frac{v_w}{v_s}\right)} \tag{31}$$

Since θ is small, the second term is ignored, then:

$$l_k = \left(1 \pm \frac{v_w}{v_s}\right) l_e \tag{32}$$

As seen in Sect. 3.2, the variation process of the grinding force can be fitted according to the actual cutting length l_k of the abrasive grain and the maximum grinding force during the cutting process of the abrasive grain.

3.3.2 Prediction of grinding force for grinding head

To accurately predict the grinding force of the grinding head during the grinding process, it is necessary to establish a surface topography model of the grinding head. This model is used to analyze the positions and states of the abrasive grains in the instantaneous grinding region to obtain the instantaneous grinding force generated by each abrasive grain. The grinding force for the grinding head is considered to be the sum of the grinding forces generated by all abrasive grains within the grinding arc region. Figure 16 illustrates the process flowchart for modeling the grinding force of the grinding head.

First, the variation patterns of abrasive grain size, number, distribution spacing, and protruding height obtained from the measurement analysis in Sect. 2.2 are taken as input parameters. A virtual grinding head model that closely resembles the actual grinding head surface is generated. Then, a kinematic analysis is performed on the generated grinding head model based on the machining parameters to calculate the static contact arc length, dynamic contact arc length, and maximum undeformed chip thickness of each abrasive grain. Next, the grinding arc region is analyzed at each moment. The size, attitude, and maximum undeformed chip thickness of the active abrasive grains within the grinding arc region are substituted into an empirical formula, along with the dynamic contact arc length, to obtain the grinding force curve for a single abrasive grain. By correlating the instantaneous position of the abrasive grain with the grinding force curve, the instantaneous grinding force of the abrasive grain can be determined. Finally, the instantaneous grinding forces of all active abrasive grains within the grinding arc region are summed to obtain the instantaneous grinding force value of the grinding head.

In order to analyze the grinding arc region at each moment of the grinding process, the grinding head is divided into n_t regions according to the grinding parameters, as shown in Fig. 17, where n_t is the ratio of the perimeter πd_e of the grinding head to the length l_e of the grinding arc. When the grinding head is grinding the workpiece, the grinding arc region at any moment can be considered as the part of the grinding head where a certain region overlaps with the workpiece. For the surface of the grinding head, each region of the abrasive grain characteristics and distribution is different, resulting in each region of the effective number of abrasive grains and single-grain grinding force to have significant differences, thus affecting the value of the grinding force of the grinding head at different times. The fluctuation curve of the grinding force during the grinding process can be obtained by analyzing and calculating the grinding force corresponding to different areas.

4 Experimentation

In order to validate the grinding force prediction model proposed in this paper, experiments on grinding Inconel 718, a nickel-based superalloy, with a grinding head are required.

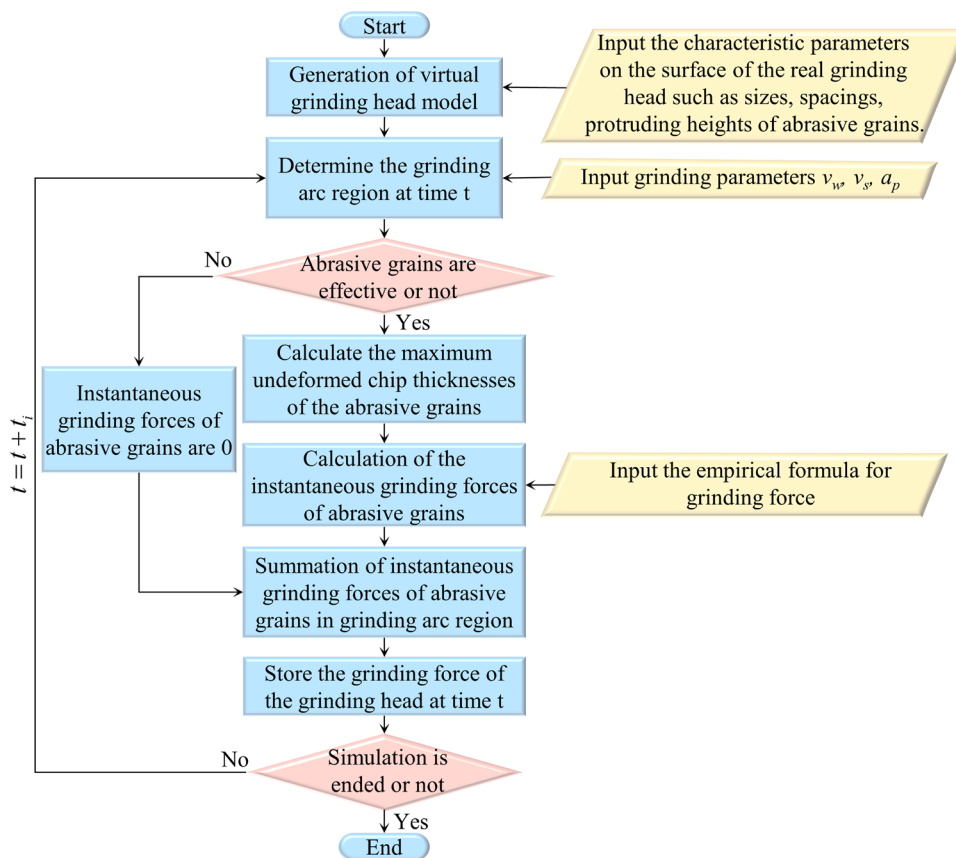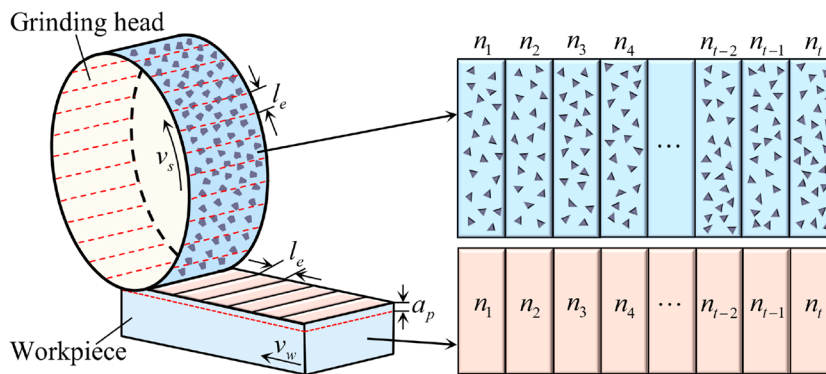**Fig. 16** Flowchart for modeling grinding force of grinding head

**Fig. 17** Variation mechanism of grinding force

4.1 Experimental setup and program

The workpiece selected for experimentation was a size 74mm × 74mm nickel-based superalloy Inconel 718 with a grinding width of 4 mm. In order to ensure precise control of the grinding width, the workpiece was designed with an overhanging state and fixed to the sensor using screws, as shown in Fig. 18a. The experiment utilized a 100# plated CBN grinding head with a 16-mm diameter to ensure consistency with the predicted model in terms of abrasive grain characteristics and distribution. Before the

experiment, the workpiece surface was polished to prevent any influence from previous processing traces.

The experiment utilized the DYDW-100-type six-axis force sensor for measuring force. This sensor has a measurement range of 200 N, a measurement accuracy of 0.001 N, and allows a maximum of five times overload. The measurement signals from the force sensor are transmitted to the D.R304-type multi-component sensor signal processor, which amplifies, filters, decouples, converts, and corrects the sensor output signals. The processor transfers the required grinding force data for the experiment to the host computer

Fig. 18 Grinding experimental equipment

(a) Assembly position of electroplated grinding head and workpiece

(b) Signal processor
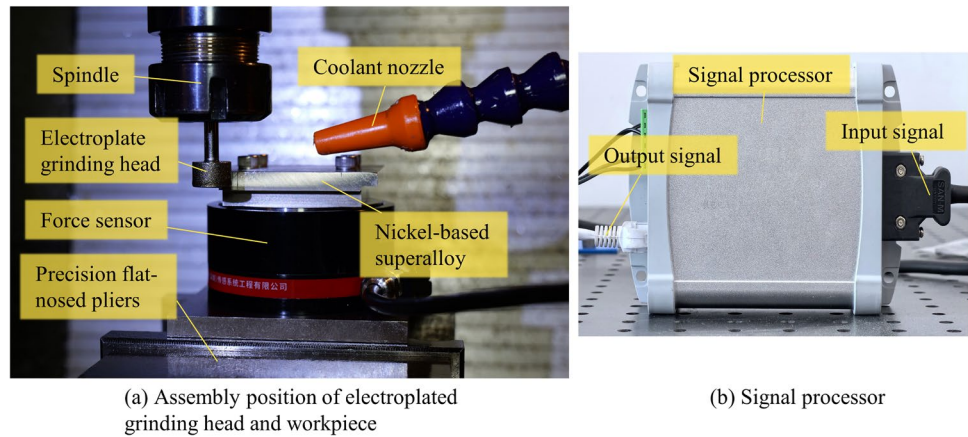
via an ethernet interface, as shown in Fig. 18b. The sampling rate for measuring grinding force during the experiment is set at 1 kHz.

The grinding experiments were conducted on a VC600 CNC machine tool, with a maximum spindle speed of 8000 rpm, a maximum feed speed of 10000 mm/min, and a positioning accuracy of 0.001 mm. Before the experiment, the connecting body of the sensor and the workpiece were fixed on the CNC machine tool with precision flat-nosed pliers. Due to the high temperatures generated during the grinding of nickel-based superalloys, which can easily lead to abrasive grain detachment from the grinding head surface and workpiece surface burnout, a wet grinding experiment was used. Multiple groups of grinding experiments were conducted to minimize experimental error with varying grinding depths, feed speeds, and rotational speeds of the grinding head. Some of the experimental process parameters are shown in Table 5.

4.2 Experimental results analysis

In order to fully demonstrate the effectiveness of the proposed method in predicting grinding forces, a comparison was made between the grinding forces predicted by the method in this paper and the grinding forces measured in grinding experiments. Figure 19 shows the overall comparison of grinding forces for some parameters. It can be observed that the predicted grinding forces show certain fluctuations compared to the experimental grinding forces, and this is because the sampling rate of the force sensor is relatively low, resulting in long sampling intervals that cannot capture the continuous changes in grinding forces during the individual grinding process of each abrasive grain. Therefore, it cannot accurately reflect real-time variations in grinding forces during the grinding process. However, under different machining parameters, the moving average curve of the predicted grinding forces (PMAC) closely matches the moving average curve

Table 5 Grinding experimental process parameters

Number	Rotational speeds of the grinding head (rpm)	Feed speed (mm/min)	Grinding depth (mm)
1	4000	60	0.03
2	4000	90	0.04
3	4000	120	0.05
4	4000	150	0.06

of the experimental grinding forces (EMAC). The overall fluctuation range of both curves is essentially the same. It indicates the feasibility and accuracy of the proposed prediction method in this paper to a large extent.

The grinding force curve is complex and variable, making it difficult to directly validate the effectiveness of the prediction method in numerical terms. Therefore, the grinding force data needs to be averaged and quantified. Figure 20 shows a numerical comparison of the grinding force for some parameters. It can be observed that the overall error of the tangential grinding force in the x-direction does not exceed 11.44%, with an average error of 7.42%, and the overall error of the normal grinding force in the y-direction does not exceed 14.25%, with an average error of 9.77%. The average prediction error is lower than those of the previous models with an average deviation in the range of 8–14% [14, 19, 20]. These results demonstrate the accuracy of the grinding force prediction method. The sources of error are:

1. In order to facilitate the simulation analysis, the model still simplified the surface topography of the grinding head.
2. The finite element simulation did not consider the effect of temperature changes during cutting on material mechanical properties, such as changes in material elastic modulus with temperature.

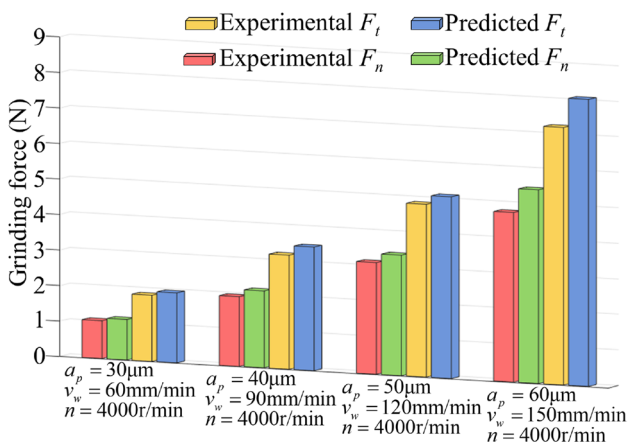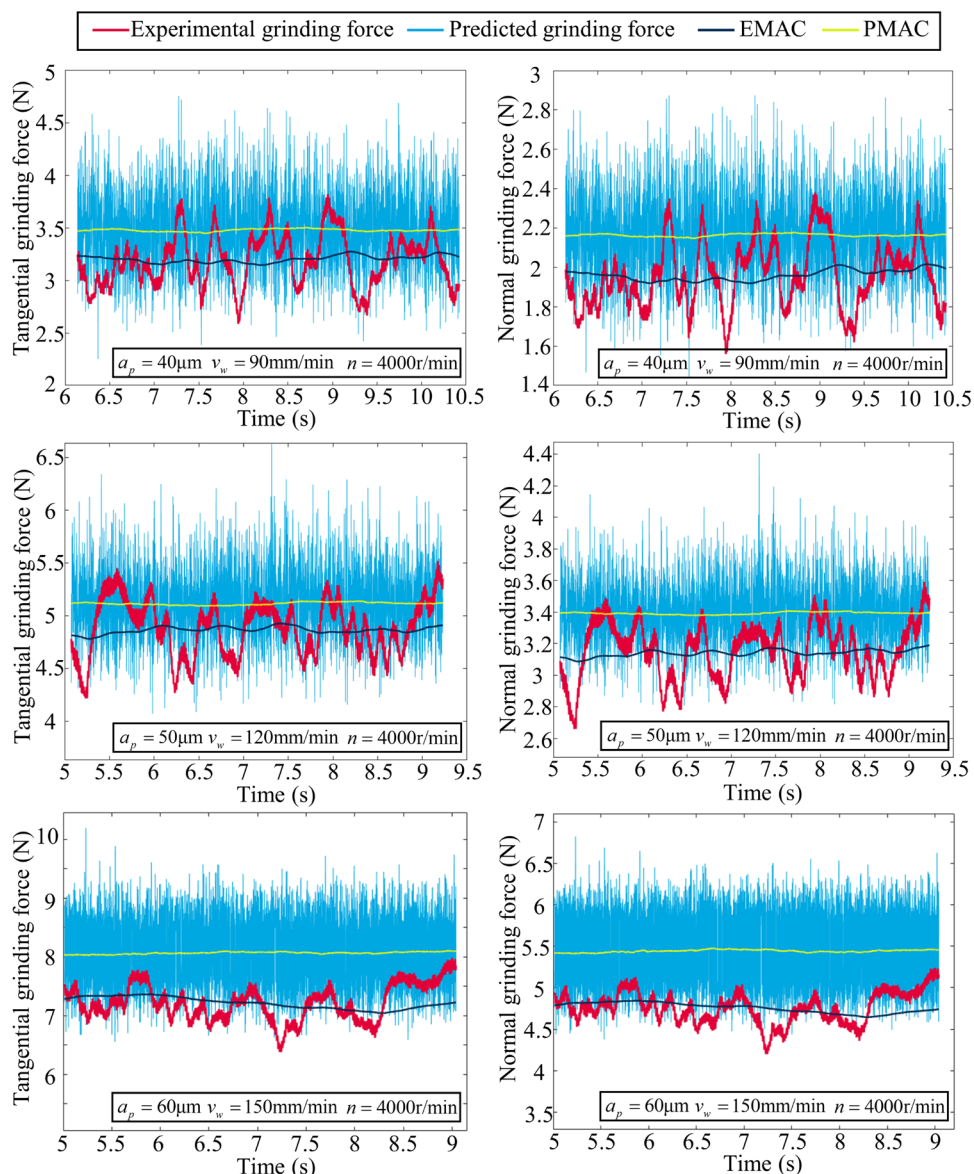Fig. 19 Comparison between predicted grinding force and experimental grinding force

Fig. 20 Average value of predicted grinding force and experimental grinding force

3. Complex situations may arise during grinding experiments, such as abrasive grain wear, detachment, and workpiece deformation, which cannot be accurately predicted.

4. The predictive model only analyzed the interference between abrasive grains and the workpiece without considering the influence between abrasive grains. For adjacent abrasive grains along the circumferential direction of the grinding head, whether the latter abrasive grain interferes with the workpiece depends on the distance and protruding height difference between the former and latter abrasive grains. It can result in the predicted grinding forces being larger than the experimental grinding forces.

Although there is a certain error between the predicted and experimental values, the predicted grinding force is

more consistent with the experimental values regarding the overall trend and numerical quantification, which can reflect the actual grinding process. Therefore, the grinding force prediction method proposed in this paper has a certain feasibility and accuracy.

4.3 Influence of grinding parameters on grinding force

Many studies have shown that the grinding parameters are the key factors affecting the grinding force [32], and the correctness of the grinding force prediction method proposed in this study can be further verified by analyzing the influence law of grinding depth and feed speed on the grinding force.

4.3.1 Influence of grinding depth on grinding force

The variation in grinding depth directly affects the maximum undeformed chip thickness and the area of the grinding arc region during abrasive grain cutting. It is related to the grinding force of a single abrasive grain and the number of abrasive grains in the grinding arc region, ultimately affecting the final grinding force. In general, as the grinding depth increases, the grinding force gradually increases.

Figure 21 shows the average values of the predicted and experimental grinding forces at different grinding depths. It can be observed that the changing trend of the predicted grinding force is basically consistent with the experimental grinding force. As the grinding depth increases, both the tangential and normal grinding forces show a significant synchronous increase. However, the difference between the experimental and predicted values gradually increases. The main reason is that the grinding force prediction method proposed in this paper does not consider the interference of abrasive grains distributed axially on the grinding head surface during the cutting process. The cutting paths between axially adjacent abrasive grains may overlap as the grinding depth increases. The overlapped portion was not removed when predicting the grinding force, resulting in the predicted value being larger than the experimental value.

The increase in grinding force in Fig. 21 slows down as the grinding depth increases because the protruding heights of the abrasive grains on the surface of the grinding head follow a normal distribution. According to the analysis in Sect. 2.2, when the grinding depth is 30 μm, most of the abrasive grains cannot interfere with the workpiece, and at this time, the grinding force is relatively small. When the grinding depth increases to 40 μm, the number of abrasive grains interfering with the workpiece increases significantly, and the grinding force increases rapidly. As the grinding depth continues to increase, the rate of increase in the number of abrasive grains involved in the grinding process slows, and the magnitude of the increase in grinding force decreases. Since the number of
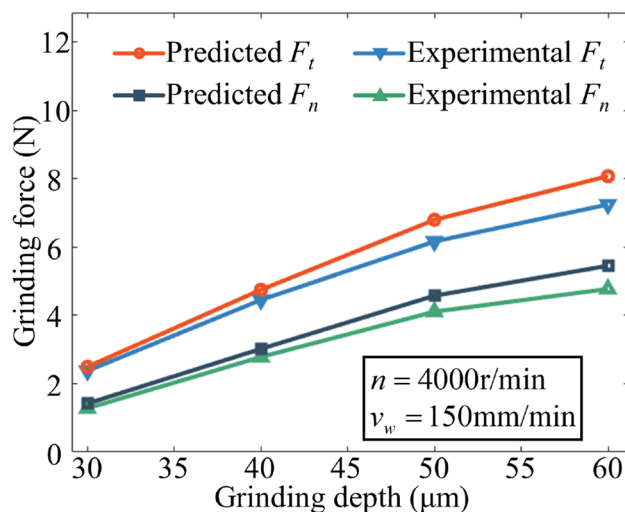

Fig. 21 Grinding forces at different grinding depths

abrasive grains on the grinding head surface is fixed, all the abrasive grains are involved in grinding when the grinding depth exceeds a critical value. At this time, as the grinding depth continues to increase beyond this critical value, the variation in grinding force gradually tends to stabilize.

4.3.2 Influence of feed speed on grinding forces

Feed speed is the basis of continuous grinding, and Fig. 22 shows the average values of predicted and experimental grinding forces at different feed speeds. As the feed speed increases, the material removal rate per unit time increases, and the undeformed chip thickness of the abrasive grains also increases. Hence, both the predicted and experimental grinding forces show an increasing trend. However, the increment is small due to the feed speed being very small compared to the rotational speed of the grinding head. According to the analysis in Sect. 3.1, it can be seen that under the premise of the rotational speed of the grinding head is unchanged, the feed speed has less influence on the thickness of the undeformed chip, and the number of abrasive grains through the grinding arc area per unit time of the increase in feed speed increases only a little. Therefore, the tangential grinding force and normal grinding force are relatively stable.

5 Results and discussion

This paper proposes a method that combines statistical analysis and finite element simulation to simulate and analyze the grinding process of different characteristic abrasive grains, aiming to predict the grinding force of the grinding head. The method establishes a single-grain model based on the surface topography of the actual grinding head, and considers the interference
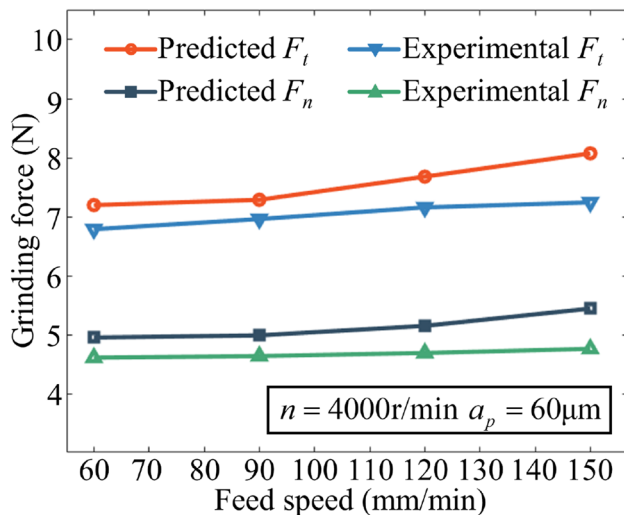
Fig. 22 Grinding forces at different feed speeds

problems in the actual grinding process as well as the material properties of the workpiece in the finite element simulation. The prediction accuracy is effectively improved, and the grinding force can be predicted quickly and intuitively. The main conclusions of this paper can be summarized as follows:

1. The microfocus measurement method can accurately reconstruct the surface morphology of the grinding head with a maximum size error of 2 μm and a maximum distribution error of 3 μm. Through measurement and analysis, it can be seen that the size, protruding height, and distribution spacing of the abrasive grains on the grinding head surface follow a normal distribution.

2. By analyzing the undeformed chip thickness of single abrasive grains based on the geometric parameters of the real abrasive grain and performing cutting simulation of different abrasive grain characteristics, the cutting process of abrasive grains can be effectively simulated, the cutting mechanism of abrasive grains can be revealed, and the real grinding process can be more accurately reproduced.

3. The predicted grinding force obtained based on single grain cutting simulation and statistical analysis can reflect the actual value of the grinding force to a certain extent. Compared with the experimental grinding force, the fluctuation range of the predicted grinding force is the same. The average error of the tangential grinding force F_t is 7.42%, and the average error of the normal grinding force F_n is 9.77%, which is more accurate than previous models.

4. The variation trend of the predicted and experimental grinding forces is the same. As the grinding depth increases, the maximum undeformed chip thickness increases, and the grinding force increases significantly, but the increase gradually becomes slower. As the work-

piece feed speed increases, the grinding force tends to increase because the value of the feed speed is relatively small, and the increment of the grinding force is small.

The grinding force prediction method can guide the industrial grinding process to a certain extent (optimize grinding parameters, improve grinding efficiency, and control the range of grinding force). In order to make the prediction results more accurate, it is also necessary to further analyze the interference problem between the abrasive grains and abrasive grains and the workpiece during the grinding process of the grinding head, which is more consistent with the actual grinding process.

Declarations

References

1. Kang MX, Zhang L, Tang WC (2020) Study on three-dimensional topography modeling of the grinding wheel with image processing techniques. Int J Mechan Sci 167:105241. https://doi.org/10.1016/j.ijmecsci.2019.105241

2. Meng QY, Guo B, Zhao QL, Li HN, Jackson MJ, Linke BS, Luo XC (2023) Modelling of grinding mechanics: a review. Chinese J Aeronaut 36(7):25–39. https://doi.org/10.1016/j.cja.2022.10.006

3. Mishra VK, Salonitis K (2013) Empirical estimation of grinding specific forces and energy based on a modified Werner grinding

model. Procedia CIRP 8:287–292. https://doi.org/10.1016/j.procir.2013.06.104

4. Wang YQ, Li XL, Wu YQ, Mu DK, Huang H (2021) The removal mechanism and force modelling of gallium oxide single crystal in single grit grinding and nanoscratching. Int J Mechan Sci 204:106562. https://doi.org/10.1016/j.ijmecsci.2021.106562

5. Fuh KH, Wang SB (1997) Force modeling and forecasting in creep feed grinding using improved bp neural network. Int J Mach Tools Manufact 37(8):1167–1178. https://doi.org/10.1016/S0890-6955(96)00012-0

6. Zhou H, Ding WF, Li Z, Su HH (2019) Predicting the grinding force of titanium matrix composites using the genetic algorithm optimizing back-propagation neural network model. Proceed Instit Mechan Eng, Part B: J Eng Manufact 233(4):1157–1167. https://doi.org/10.1177/0954405418780166

7. Zhang LF, Wang S, Li Z, Qiao WL, Wang Y, Wang T (2019) Influence factors on grinding force in surface grinding of unidirectional C/SiC composites. Appl Comp Mater 26:1073–1085. https://doi.org/10.1007/s10443-019-09767-5

8. Younis MA, Alawi H (1984) Probabilistic analysis of the surface grinding process. Transact Canad Soc Mechan Eng 8(4):208–213. https://doi.org/10.1139/tcsme-1984-0031

9. Esmaeili H, Adibi H, Rizvi R, Rezaei SM (2022) Coupled thermomechanical analysis and optimization of the grinding process for Inconel 718 superalloy using single grit approach. Tribol Internat 171:107530. https://doi.org/10.1016/j.triboint.2022.107530

10. Anderson D, Warkentin A, Bauer R (2011) Experimental and numerical investigations of single abrasive-grain cutting. Int J Mach Tools Manufact 51(12):898–910. https://doi.org/10.1016/j.ijmachtools.2011.08.006

11. Yang M, Li CH, Zhang YB, Jia DZ, Li RZ, Hou YL, Gao HJ (2019) Predictive model for minimum chip thickness and size effect in single diamond grain grinding of zirconia ceramics under different lubricating conditions. Ceram Int 45(12):14908–14920. https://doi.org/10.1016/j.ceramint.2019.04.226

12. Hecker RL, Liang SY, Wu XJ, Xia P, Jin DGW (2007) Grinding force and power modeling based on chip thickness analysis. Int J Adv Manufact Technol 33:449–459. https://doi.org/10.1007/s00170-006-0473-y

13. Durgumahanti USP, Singh V, Rao PV (2010) A new model for grinding force prediction and analysis. Int J Mach Tools Manufact 50(3):231–240. https://doi.org/10.1016/j.ijmachtools.2009.12.004

14. Dai CW, Yin Z, Ding WF, Zhu YJ (2019) Grinding force and energy modeling of textured monolayer CBN wheels considering undeformed chip thickness nonuniformity. Int J Mechan Sci 157:221–230. https://doi.org/10.1016/j.ijmecsci.2019.04.046

15. Li BK, Dai CW, Ding WF, Yang CY, Li CH, Kulik O, Shumyacher V (2021) Prediction on grinding force during grinding powder metallurgy nickel-based superalloy FGH96 with electroplated CBN abrasive wheel. Chinese J Aeronaut 34(8):65–74. https://doi.org/10.1016/j.cja.2020.05.002

16. Liu MZ, Li CH, Zhang YB, Yang M, Gao T, Gui X, Wang XM, Xu WH, Zhou ZM, Liu B, Said Z, Li RZ, Sharma S (2023) Analysis of grinding mechanics and improved grinding force model based on randomized grain geometric characteristics. Chinese J Aeronaut 36(7):160–193. https://doi.org/10.1016/j.cja.2022.11.005

17. Setti D, Kirsch B, Aurich JC (2017) An analytical method for prediction of material deformation behavior in grinding using single grit analogy. Procedia CIRP 58:263–268. https://doi.org/10.1016/j.procir.2017.03.193

18. Yang ZY, Chu Y, Xu XH, Huang HJ, Zhu DH, Yan SJ, Ding H (2021) Prediction and analysis of material removal characteristics for robotic belt grinding based on single spherical abrasive grain model. Int J Mechan Sci 190:106005. https://doi.org/10.1016/j.ijmecsci.2020.106005

19. Li HN, Yu TB, Wang ZX, Zhu LD, Wang WS (2017) Detailed modeling of cutting forces in grinding process considering variable stages of grain-workpiece micro interactions. Int J Mechan Sci 126:319–339. https://doi.org/10.1016/j.ijmecsci.2016.11.016

20. Jamshidi H, Budak E (2020) An analytical grinding force model based on individual grit interaction. J Mater Process Technol 283:116700. https://doi.org/10.1016/j.jmatprotec.2020.116700

21. Wang XZ, Liu QY, Zheng YH, Xing W, Wang MH (2022) A grinding force prediction model with random distribution of abrasive grains: considering material removal and undeformed chips. Int J Adv Manufact Technol 120(11-12):7219–7233. https://doi.org/10.1007/s00170-022-09213-0

22. Meng QY, Guo B, Wu GC, Xiang Y, Guo ZF, Jia JF, Zhao QL, Li KN, Zeng ZQ (2023) Dynamic force modeling and mechanics analysis of precision grinding with microstructured wheels. J Mater Process Technol 314:117900. https://doi.org/10.1016/j.jmatprotec.2023.117900

23. Wu ZH, Zhang LC (2023) Analytical grinding force prediction with random abrasive grains of grinding wheels. Int J Mechan Scie 250:108310. https://doi.org/10.1016/j.ijmecsci.2023.108310

24. Setti D, Ghosh S, Rao PV (2017) A method for prediction of active grits count in surface grinding. Wear 382:71–77. https://doi.org/10.1016/j.wear.2017.04.012

25. Tang JJ, Qiu ZJ, Li TY (2019) A novel measurement method and application for grinding wheel surface topography based on shape from focus. Measurement 133:495–507. https://doi.org/10.1016/j.measurement.2018.10.006

26. Fu DK, Ding WF, Miao Q, Xu JH (2017) Simulation research on the grinding forces and stresses distribution in single-grain surface grinding of Ti-6Al-4V alloy when considering the actual cutting-depth variation. Int J Adv Manufact Technol 91:3591–3602. https://doi.org/10.1007/s00170-017-0084-9

27. Li X, Guan CM, Zhao P (2018) Influences of milling and grinding on machined surface roughness and fatigue behavior of GH4169 superalloy workpieces. Chinese J Aeron 31(6):1399–1405. https://doi.org/10.1016/j.cja.2017.07.013

28. Rao ZW, Xiao GD, Zhao B, Zhu YJ, Ding WF (2021) Effect of wear behaviour of single mono- and poly-crystalline cBN grains on the grinding performance of Inconel 718. Ceram Int 47(12):17049–17056. https://doi.org/10.1016/j.jmapro.2018.09.023

29. Bartolomeis AD, Newman ST, Jawahir IS, Biermann D, Shokrani A (2021) Future research directions in the machining of Inconel 718. J Mater Process Technol 297:117260. https://doi.org/10.1016/j.jmatprotec.2021.117260

30. Erice B, Gálvez F (2014) A coupled elastoplastic-damage constitutive model with Lode angle dependent failure criterion. Int J Solids Struct 51(1):93–110. https://doi.org/10.1016/j.ijsolstr.2013.09.015

31. Nasr MNA, Ammar MMA (2017) An evaluation of different damage models when simulating the cutting process using FEM. Procedia CIRP 58:134–139. https://doi.org/10.1016/j.procir.2017.03.202

32. Dai CW, Ding WF, Zhu YJ, Xu JH, Yu HW (2018) Grinding temperature and power consumption in high speed grinding of Inconel 718 nickel-based superalloy with a vitrified CBN wheel. Precis Eng 52:192–200. https://doi.org/10.1016/j.precisioneng.2017.12.005